Tomographic inversion of gravity gradient field for a synthetic Itokawa model

Liisa-Ida Sorsa [a,*], Mika Takala [a], Patrick Bambach [b], Jakob Deller [b], Esa Vilenius [b], Jessica Agarwal [b], Kieran A. Carroll [c], Özgür Karatekin [d], Sampsa Pursiainen [a]

[a] *Tampere University, Faculty of Information Technology and Communication Sciences, PO Box 1001, 33014 Tampere University, Finland*
[b] *Max Planck Institute for Solar System Research, Justus-von-Liebig-Weg 3, 37077 Göttingen, Germany*
[c] *Gedex Systems Inc., 407 Matheson Blvd. East, Mississauga, Ontario L4Z 2H2, Canada*
[d] *Royal Observatory of Belgium (ROB), Avenue Circulaire 3, Brussels 1180, Belgium*

ARTICLE INFO

ABSTRACT

This article investigates reconstructing the internal mass density of a numerical asteroid model using the gradient of a simulated gravity field as synthetic measurement data. Our goal is to advance the mathematical inversion methodology and find feasibility constraints for the resolution, noise and orbit selection for future space missions. We base our model on the shape of the asteroid Itokawa as well as on the recent observations and simulation studies which suggest that the internal density varies, increasing towards the center, and that the asteroid may have a detailed structure. We introduce randomized multiresolution scan algorithm which might provide a robust way to cancel out bias and artifact effects related to the measurement noise and numerical discretization. In this scheme, the inverse algorithm can reconstruct details of various sizes without fixing the exact resolution *a priori*, and the randomization minimizes the effect of discretization on the solution. We show that the adopted methodology provides an advantageous way to diminish the surface bias of the inverse solution. The results also suggest that a noise level below 80 Eotvos will be sufficient for the detection of internal voids and high density anomalies, if a sparse set of measurements can be obtained from a close-enough distance to the target.

1. Introduction

Geophysical investigations into the subsurface of the Earth are nowadays based on combining information of multiple geophysical fields, leading to more reliable models of the subsurface structures (Erkan and Jekeli, 2011) . For example, subsurface cavities have been successfully detected by combining gravity field and ground penetrating radar measurements (Chromk et al., 2016; Mochales et al., 2008; Panisova et al., 2013) . Furthermore, gravity gradiometry has been shown to detect local mass or density anomalies (Erkan and Jekeli, 2011; Jekeli and Lian Abt, 2011; McKenna et al., 2016) . These investigations commonly have a low signal-to-noise ratio, hence the need to combine data from various measurement techniques. Such multi-modal approach is used to maximize the probability of anomaly detection and minimize that of a false alarm (McKenna et al., 2016) .

The first attempt to investigate the deep interior structure of a small solar system body (SSSB) was the Comet Nucleus Sounding Experiment by Radio-wave Transmission (CONSERT), a part of European Space Agency's (ESA) Rosetta mission to the comet 67P/Churyumov-Gerasimenko, in which a radio signal was transmitted between the orbiter *Rosetta* and the lander *Philae* (Kofman et al., 1998, 2015, 2007) . Other missions to asteroids have concentrated on the structure and composition of the surface of the target SSSBs. The Hayabusa mission (Japan Aerospace Exploration Agency, 2003) by the Japanese Aerospace Exploration Agency (JAXA) explored the asteroid Itokawa extensively and measured the physical, chemical and geological properties of the body from orbit (Fujiwara et al., 2006; Okada et al., 2006) . Furthermore, the Hayabusa mission returned a sample of the asteroid surface regolith for analysis on earth, confirming the classification of the asteroid to S-type (Fujiwara et al., 2006; Nakamura et al., 2011) , as was originally reported by the earth-based visible and near-infrared spectroscopy observations (Binzel et al., 2001) . Analysis of the collected dust particles suggests that Itokawa is an asteroid made of reassembled pieces of the inner portions of a once larger asteroid (Nakamura et al.,

---

2011; Tsuchiyama et al., 2011) .

The currently ongoing missions, Hayabusa2 to the asteroid 16173 Ruygu by JAXA (Tsuda et al., 2013) and OSIRIS-REx to the asteroid 101955 Bennu by NASA (Lauretta et al., 2017) have been designed to measure the physical, chemical and geological properties of the target asteroids.

Based on the experience obtained in terrestrial applications (Chromk et al., 2016; Erkan and Jekeli, 2011; Mochales et al., 2008), the future missions to explore the interior structure of SSSBs would benefit from combining measurements from more than one geophysical field. Our recently published simulation studies of equipping CubeSats with a low-frequency stepped-frequency radar (Sorsa et al., in press; Takala et al., in press) suggest that tomographic reconstruction of the full electromagnetic wavefield can reveal internal structural anomalies in an SSSB. Therefore, augmenting such radar measurements with gravity field measurements by gradiometry presents an interesting opportunity to obtain complementary information on the structure of the target. Such a gravity gradiometer instrument has been suggested, for example, by the recent studies (Carroll and Faber, 2018; Carroll et al., 2018) . A combined gravity and radar measurement for interior investigation of an SSSB is, for example, a part of ESA's future mission plan HERA (Karatekin and Goldberg, 2018) . The gravity field can be sensed via a direct measurement by a gravity gradiometer (Carroll and Faber, 2018) or indirectly by observing the Doppler shift of a radio signal transmitted by a spacecraft (Andrews-Hanna et al., 2013; Konopliv et al., 2013) . The recent Moon Gravity Recovery and Internal Laboratory (GRAIL) mission used the latter method to measure the change in the distance between two co-orbiting spacecrafts as they flew above the lunar surface to calculate the gravitational potential from the spherical harmonics data set (Zuber et al., 2013) .

In this paper, we investigate inversion of simulated gravity measurements obtained for a synthetic asteroid model which is based on the shape of the asteroid Itokawa and augmented with interior density anomalies. Our model relies on the recent observations and impact simulations which suggest that the internal density of asteroids varies, increasing towards the center, and that the interior may have a detailed structure in which void cavities and cracks have been formed in between rubble or larger boulders (Carry, 2012; Deller, 2017; Jutzi and Benz, 2017) . Our goal is to advance the mathematical inversion methodology and find feasibility constraints for the resolution of the reconstruction, noise and orbit selection to guide the design of future space missions. We introduce and investigate a randomized multiresolution scan algorithm which might provide a robust way to cancel out bias and artifact effects related to the measurement noise and numerical discretization. In this scheme, the inverse algorithm can reconstruct details of various sizes without fixing the exact resolution *a priori*, and the randomization minimizes the effect of discretization on the solution. We show that the adopted methodology provides an advantageous way to diminish the surface bias of the inverse solution. The results also suggest that a noise level below 80 Eotvos will be sufficient for the detection of internal voids and high density anomalies, if a sparse set of measurements can be obtained from a close-enough distance to the target.

2. Materials and methods

We use the gradient of the scalar gravity field strength as input data for our inversion procedure and study how the quality of the reconstruction depends on various parameters. We focus on the field strength for simplicity, assuming that the gravitational torsion field, which is omitted here, might involve more uncertainty, if the actual *in-situ* measurement is done under a rotational motion.

The two synthetic asteroid interior structure models have been created from the shape model of the asteroid Itokawa. The forward simulation of the field strength gradient is carried out in a uniformly regular tetrahedral finite element mesh (Braess, 2007) . The mesh is generated with respect to a uniform point (vertex) lattice by subdividing

each cube in the lattice into six tetrahedra. The synthetic measurements are investigated for two orbit radii. Sections 2.1–2.4 describe the model and procedure used to create the simulated measurements.

In the inversion stage described in Section 2.5, we use a hierarchical Bayesian model which allows adjusting the hyperprior parameter for finding a well-localized reconstruction. The inverse estimate is found through a randomized multiresolution scanning technique in which the inversion mesh is decomposed to multiple, nested levels. Using this randomized scanning algorithm with Iterative Alternating Sequential (IAS) inversion algorithm, it is possible to average out discretization errors and hence the final inverse solution is less dependent on the discretization of the computation domain than it would otherwise be.

2.1. Asteroid models

The asteroid models used in this work are based on the triangular stereolithography (STL) surface mesh (Hayabusa Project Science Data Archive, 2007) of the asteroid Itokawa (Saito et al., 2006) . The unstructured triangulated asteroid surface model was imported to Meshlab (Cignoni et al., 2008) and resampled with Poisson-disk sampling algorithm Bridson which produces a uniformly distributed set of points fulfilling a given minimum distance condition. This was done to obtain a regular surface mesh with a resolution comparable to that of the eventual volumetric mesh applied in the numerical simulations.

The asteroid model consists of a surface layer and an interior compartment in which the deep interior anomalies are located. The surface of the interior compartment was created by further downsampling the shape model and rescaling it by the factor of 0.9. The same asteroid model structure was also used in radar simulations in Sorsa et al. (in press).

The bulk density of Itokawa as measured during the Hayabusa mission is $1.9 \pm 0.13 \, \text{g/cm}^3$ and its orthogonal axes are 535, 294, and 209 m (Fujiwara et al., 2006). A careful analysis of the rotational lightcurve observations and thermophysical analysis suggest that Itokawa is composed of two bodies with different bulk densities (Lowry, S. C. et al., 2014) . A recent study on asteroid mass-concentration estimates obtained by asteroid impact simulations (Jutzi and Benz, 2017) suggests that the bulk density of the deep interior part is higher than that of the surface. To simulate these features and test tomographic inversion, we created two interior models (A) and (B) depicted in the Fig. 1.

In the Model(A), the surface and the deep interior densities were adjusted to $1.8 \, \text{g/cm}^3$ and $2.0 \, \text{g/cm}^3$, respectively. This way, we could keep the bulk density close to the measured one while accounting for density variation between the surface and the deep interior structures. Two spherical void cavities of 40 and 30 m radii and zero density were inserted into the asteroid body and the head, respectively. Based on the actual measurements of Itokawa by Hayabusa mission (Fujiwara et al., 2006) a rubble-pile asteroid may contain significant void space in the deep interior and these cavities model such anomalies. The locations were chosen so that one is in the body of the asteroid, in the deep interior part, and the other in the head, enclosed closer to the surface while being moderate in size. The center of mass of the Model(A) is in $x = 64, y = 0$, $z = 0 \, \text{m}$, assuming the center of the coordinate system is in the geometrical center of the asteroid.

In the Model(B), the densities of the surface and the interior compartments were adjusted to $1.6 \, \text{g/cm}^3$ and $1.8 \, \text{g/cm}^3$, respectively. A spherical high-density anomaly with a density of $8 \, \text{g/cm}^3$, and 45 m radius was located in the head of the asteroid, covering approximately 55 % of the total radius of the head and resulting in a total bulk density distribution similar to the findings in Lowry, S. C. et al. (2014), and a total bulk density equal to that of Model (A), $1.9 \, \text{g/cm}^3$. An internal high-density anomaly within a rubble-pile asteroid could result for example from an impact event. The center of mass of the Model(B) is in the coordinates $x = 122, y = 0, z = -16 \, \text{m}$.
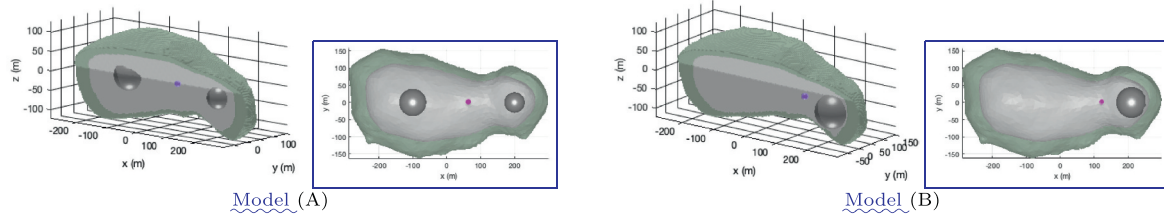
Fig. 1. 3D cut views showing the structures of the exact models (A) and (B) with their centers of mass indicated by magenta. **Left:** Model (A), the double void structure. **Right:** Model (B), the high density spherical anomaly in the head of the asteroid.

2.2. Measurement points

The measurement point sets were modelled similar to our earlier work (Sorsa et al., in press; Takala et al., in press) in which two CubeSats orbit an asteroid at a defined radius measured from the geometrical center of the asteroid. Two circular orbits with radii of 305 m and 500 m were investigated. These orbits were selected to provide initial results on the quality of reconstructions that can be achieved when performing measurements and analysis with state-of-the-art instruments and tomographic inversion methods. While the lower orbit (305 m) is not realistic for performing satellite-based measurements, it was included to provide a reference for close-proximity measurements. The angular coverage between the measurement plane and the asteroid spin axis (here: spin around the z axis in the xy plane) was set to 70 or 30 °, resulting in the limited-angle spatial coverage of measurement points depicted in the Fig. 2, with apertures around the z-axis.

In practice, the gravity field measurements take time to carry out, resulting in measurement arcs rather than points. The effect of measurement arcs on the reconstructions was analyzed by introducing positional uncertainty in the model via rotating the measurement point set in comparison to the background model. Two rotation angles, 5° and 10°, corresponding to realistic measurement times in the 500 m radius orbit (Table 1) were investigated. The orbit velocity was assumed to follow the equation $v = \sqrt{(GM/r)}$, in which G is Newton's gravitational constant, M the bulk mass of the asteroid and r the orbit radius. The difference between the spacecraft orbit period and the spin rate of Itokawa (12.1 h, Fujiwara et al., 2006) resulted in approximately 5% positional uncertainty in the 500 m orbit radius case. The difference between the spacecraft orbit velocity and the asteroid spin rate in the lower orbit is too large (99%) for a meaningful examination of reconstruction effects.

2.3. Measurement noise

We apply the recent noise estimate (Carroll and Faber, 2018) obtained for the VEGA space gravimeter, when it is assumedly held by a 2.5 m boom attached to the mothership of the proposed HERA mission. Akin to Carroll and Faber (2018), the measurement noise distribution is assumed to be a Gaussian zero-mean random variable to account for

Table 1
The rotation angles and measurement durations resulting from realistic measurement arcs for the investigated orbits. The rotation angles are used in investigating the effect of measurement positional uncertainty in the inversion stage.

Rotation angle	305 m orbit Duration (s)	500 m orbit Duration (s)
5°	610 s	11,814 s
10°	1220 s	23,628 s

several independent, identically distributed sources of noise. The root mean square (RMS) error estimate relating to the standard deviation σ of a Gaussian random variable obtained in the study (Carroll and Faber, 2018) is of the form

$$\sigma \approx \frac{1}{\sqrt{\tau}}\ 300\ \text{E}. \tag{1}$$

Here, τ refers to the duration of the measurement in seconds. The unit E is eotvos ($1\ \text{E} = 1\text{e}-9\ \text{s}^{-2}$). The RMS values of this study and the required measurement times calculated according to Eq. (1) can be found in Table 2. The measurement durations for the higher noise levels shown in the Table 2 are unrealistically short from a measurement time perspective, as the shortest measurement time for the instrument is 30 s (Carroll and Faber, 2018). Therefore, they have been marked in parenthesis and are included for consistency.

The RMS noise level of the VEGA instrument is 55 E resulting in a

Table 2
The measurement noise levels investigated in this study. The level of the noise and the duration required by the measurement have been estimated according to Carroll and Faber (2018). The measurement times in (c) and (d) are unrealistically short and have therefore been marked in parenthesis only for consistency.

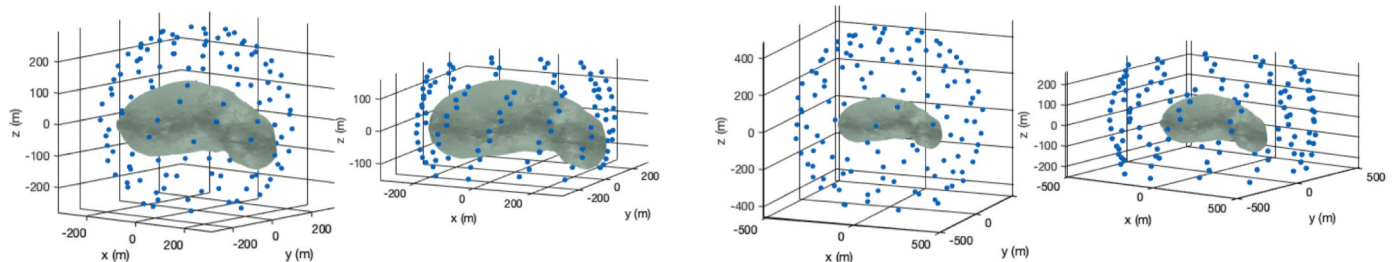| Item	RMS (E)	Duration (s)
(a)	2	2.3E4
(b)	8	1400
(c)	80	(14)
(d)	800	(0.14)

Fig. 2. **Left:** Measurement radius 305 m from the geometrical center of the asteroid, resulting in a subset of points which are very close to the surface in the long axis, limiting angle (the angle between the) 70° on the left, and 30° on the right. **Right:** Measurement radius 500 m from the center of the asteroid. Limiting angles 70° on the left, and 30° on the right.

measurement time of 27.4 s (Carroll and Faber, 2018). These finite measurement times follow from the repetitive measurement process required to measure the gradient of the gravitational field strength with a given accuracy.

From the inversion viewpoint, the measurement noise constitutes one significant error source, the other one being the modelling uncertainty related to, e.g., the position and orientation of the measurement instrument as well as the discretization of the computation domain. The methods for treating the positional error in this work are discussed more in the Section 2.5.2 which shows that the errors relating to the positional uncertainty can be decreased by a randomization and averaging procedure in the inversion stage.

2.4. Forward model

The relationship between a given mass density and the measurement data can be presented via a linear forward model of the form

$$\mathbf{y} = \mathbf{L}\mathbf{x} + \mathbf{n}, \qquad (2)$$

in which $\mathbf{x} \in \mathbb{R}^N$ is the difference between the actual mass density, i.e., the unknown of the inverse problem, and an initial guess; $\mathbf{y} \in \mathbb{R}^M$ represents the difference between the actual measurements and numerically simulated data obtained for the initial mass density; $\mathbf{L}$ is the system matrix representing the forward map; and $\mathbf{n} \in \mathbb{R}^M$ is the noise vector.

We assume that the target has been decomposed into a finite number of disjoint elements $T_1, T_2, \ldots, T_m$ (here: tetrahedra), and that the mass density is a piecewise constant distribution with respect to a set of disjoint subsets denoted by $R_1, R_2, \ldots, R_N$ consisting of $K_{j_1}, K_{j_2}, \ldots, K_{j_N}$ elements, respectively, with $m = \sum_{j=1}^{N} K_j$. The subset R_j is defined as the union of the elements with center of mass closest to the point $\overrightarrow{z}_j$ in the set $\overrightarrow{z}_1, \overrightarrow{z}_2, \ldots, \overrightarrow{z}_N$ of randomly generated points.

The characteristic function of the element T_j, which is equal to one within the set j and zero elsewhere, is denoted by χ_j. The resulting mass difference density, $\Delta\rho$, is of the form

$$\Delta\rho = \sum_{j=1}^{N} x_j \psi_j \quad \text{with} \quad \psi_j = \sum_{k_j=1}^{K_j} \chi_j. \qquad (3)$$

The $\psi_1, \psi_2, \ldots, \psi_N$ is the function basis of the mass difference density, which is assumed to have a piecewise constant distribution inside the target asteroid. It is also the function basis for the inversion process.

Our data corresponds to the gradient of the scalar gravity field strength, i.e., the Euclidean norm of the three-component gravity field at a given point. The measurements are assumed to contain additive zero-mean Gaussian noise. Furthermore, the noise entries are assumed to be independent and identically distributed. The resulting forward model is of the form

$$
\begin{aligned}
y_i &= G \int_\Omega \Delta\rho(\overrightarrow{z}) \nabla_{\overrightarrow{r}_i} \frac{1}{\| \overrightarrow{z} - \overrightarrow{r}_i \|^2} \, d\overrightarrow{z} + n \\
&= 2G \int_\Omega \Delta\rho(\overrightarrow{z}) \frac{\overrightarrow{z} - \overrightarrow{r}_i}{\| \overrightarrow{z} - \overrightarrow{r}_i \|^4} \, d\overrightarrow{z} + n_i, \qquad (4)
\end{aligned}
$$

where y_i with $i = 1, 2, \ldots, M$ represents the difference data at the point $\overrightarrow{r}_i$; n_i is a noise vector; and G is Newton's gravitational constant.

Substituting Eq. (3) into Eq. (4) and evaluating the gradient results in the equation

$$
\begin{aligned}
y_i &= 2G \sum_{j=1}^{N} x_j \int_\Omega \psi_j \frac{\overrightarrow{z} - \overrightarrow{r}_i}{\| \overrightarrow{z} - \overrightarrow{r}_i \|^4} \, d\overrightarrow{z} + n_i \\
&= 2G \sum_{j=1}^{N} x_j \sum_{k_j=1}^{K_j} \frac{\overrightarrow{z}_{k_j} - \overrightarrow{r}_i}{\| \overrightarrow{z}_{k_j} - \overrightarrow{r}_i \|^4} \int_{T_{k_j}} d\overrightarrow{z} + n_i, \qquad (5)
\end{aligned}
$$

where $\overrightarrow{z}_{k_j}$ is the center of mass and $\int_{T_j} dz$ the volume of T_j. The resulting matrix equation is of the form Eq. (2) with the matrix $\mathbf{L} \in \mathbb{R}^{M \times N}$ given by

$$L_{i,j} = 2G \sum_{k_j=1}^{K_j} \frac{\mathbf{z}_{k_j} - \mathbf{r}_i}{\| \mathbf{z}_{k_j} - \mathbf{r}_i \|^4} \int_{T_j} d\mathbf{z}. \qquad (6)$$

2.5. Inversion process

We approach the inverse problem via the hierarchical Bayesian model (HBM) in which the unknown parameter $\mathbf{x}$ obeys a *posterior* probability density determined by the product $p(\mathbf{x}, \theta | \mathbf{y}) \propto p(\mathbf{x}, \theta) \, p(\mathbf{y} | \mathbf{x})$ between the prior density $p(\mathbf{x}, \theta)$, and the likelihood function $p(\mathbf{y} | \mathbf{x})$. The prior is a joint density of the form $p(\mathbf{x}, \theta) \propto p(\theta) \, p(\mathbf{x} | \theta)$, where the conditional part $p(\mathbf{x} | \theta)$ is a zero mean Gaussian density with a diagonal covariance matrix predicted by the hyperprior $p(\theta)$. The hyperprior is long-tailed, meaning that $\mathbf{x}$ is likely to be a sparse vector with only few entries differing from zero. For this prior structure, HBM is advantageous for finding a well-localized reconstruction. As a hyperprior, one can use either the gamma or inverse gamma density (Calvetti et al., 2009), whose shape and scale are controlled by the parameters β and θ_0, respectively. The likelihood follows directly from the measurement noise density via $\mathbf{n} = \mathbf{y} - \mathbf{L}\mathbf{x}$ with independent entries.

2.5.1. IAS inversion

The inverse estimate is found using the IAS *maximum a posteriori* (MAP) estimation method (Calvetti et al., 2009; Calvetti and Somersalo, 2008; Pursiainen and Kaasalainen, 2013). The gamma density is applied as the hyperprior. The IAS algorithm finds the MAP estimate via alternating the conditional posteriors $p(\mathbf{x} | \theta, \mathbf{y})$ and $p(\theta | \mathbf{x}, \mathbf{y})$ as the objective function. This is advantageous, since the maximizer for the first one can be found by solving a regularized least-squares optimization problem, and for the second one via an explicit analytical formula. When IAS inversion is applied with gamma density as the hyperprior, the outcome of the algorithm can be shown to correspond to the classical ℓ^2-norm regularized solution of the inverse problem.

2.5.2. Randomized multiresolution scan

In order to minimize the effect of the selected function basis $\psi_1, \psi_2, \ldots, \psi_N$ on the final reconstruction, we use a randomized multiresolution scan algorithm which finds the final reconstruction $\overline{\mathbf{x}}$ as an average $\mathbf{x}$-component of MAP estimates for $\zeta = (\mathbf{x}, \theta)$ obtained for multiple different resolution levels (Fig. 3) and randomized decompositions of the parameter space. Each decomposition is formed by selecting uniformly distributed number of points other than the selected mesh points with a nearest neighbor interpolation. Fig. 3 shows schematically one possible randomized decomposition for two resolution levels.

A decomposition D_ℓ refers to a surjective mapping $\mathbb{R}^N \to \mathbb{R}^K_\ell$ which is obtained by associating each basis function of the parameter space with the closest point in a set of K_ℓ random uniformly distributed points $\overrightarrow{p}_1, \overrightarrow{p}_2, \ldots, \overrightarrow{p}_{K_\ell}$. Each decomposition is organized into a sequence of subsets $S = \{B_1, B_2, \ldots, B_L\}$ in which the resolution, i.e., the number of randomized points grows along with ℓ as given by $K_\ell = K s^{(\ell-L)}$, where s is a user-
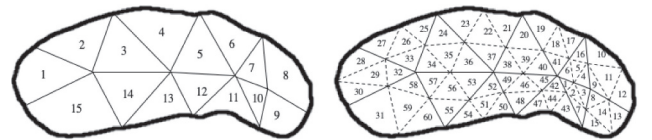

Fig. 3. A schematic illustration of subdivision of the asteroid shape into coarse (left) and fine (right) resolution subdomains. In this case the sparsity factor s, the ratio between the number of subdomains for two consecutive resolution levels, is four (4). An example of a surjective mapping from the coarse to fine resolution, $\mathbb{R}^N \to \mathbb{R}^K_\ell$, is given by $\{2\} \to \{25, 26, 27, 33\}$.

defined sparsity factor. Such a sequence is referred here to as a randomized multiresolution decomposition (Fig. 3). For optimizing the performance of the MAP estimation process, it is essential to begin with a coarse resolution and gradually proceed towards a finer one, since the distinguishability of the coarse density fluctuations which are realistic in asteroids is generally superior to that of other details such as small and well-localized density changes. The MAP estimate for $B_\ell + 1$ is obtained by using the one for B_ℓ as the initial guess (Fig. 4). Analogously, the estimate obtained for a single subset sequence is used as the initial guess for the next one. The initial guess of the whole procedure is set to be $\mathbf{x}^{(0)} = (0,0,\ldots,0)$ and $\boldsymbol{\theta}^{(0)} = (\theta_0,\theta_0,\ldots,\theta_0)$.

The algorithm proceeds as follows:

1. Choose the desired number of the resolution levels L and the sparsity factor s, i.e., the ratio of source counts between the levels.
2. For each resolution level $\ell = 1,2,\ldots,L$, create a random uniformly distributed set of center points $\vec{p}_1, \vec{p}_2, \ldots, \vec{p}_{K_\ell}$. Find the sequence of subsets $B_1, B_2, \ldots, B_{K_\ell}$ by applying the nearest interpolation scheme with respect to the center points.
3. Repeat the first two steps to generate a desired number D of independent randomized multiresolution decompositions $S_1, S_2, \ldots, S_D$.
4. Start the reconstruction process with the decomposition S_1 and an initial guess $\zeta^{(0)}$ corresponding to $\mathbf{x}^{(0)} = (0,0,\ldots,0)$ and $\boldsymbol{\theta}^{(0)} = (\theta_0,\theta_0,\ldots,\theta_0)$.
5. For decomposition S_k, find a reconstruction $x^{(\ell)}$ with an inversion technique chosen by the user, here the IAS method, and the initial guess $\zeta^{(\ell-1)}$ for the resolution levels $\ell = 1,2,\ldots,L$.
6. For level L, obtain the final estimate for the decomposition (basis) k as the normalized mean

$$\overline{\zeta}^{(k)} = \sum_{\ell=1}^{L} \zeta^{(\ell)} \Big/ \sum_{\ell=1}^{L} s^{(L-\ell)}. \tag{7}$$

Here, the denominator follows from balancing out the effect of the multiplied source count which follows from the interpolation of a coarse level estimate to a denser resolution level.

7. If $k < D$ update $k \to k + 1$, i.e. move to the next decomposition, and repeat the 5-th and 6-th step with the initial guess $\overline{\zeta}^{(k-1)}$ for the resolution level $\ell = 1$.
8. Obtain the final reconstruction $\overline{\overline{\mathbf{x}}}$ as the $\mathbf{x}$-component of the mean:

$$\overline{\overline{\zeta}}^{(k)} = \frac{1}{D} \sum_{k=1}^{D} \overline{\zeta}^{(k)}. \tag{8}$$

This procedure ensures that the ℓ^2 solution converges to the solution which is independent of the discretization of the computation domain and makes the solution to converge into the ℓ^2-norm regularized solution. Assuming that the possible density fluctuations due to the basis selection are random and identically distributed, the average should converge towards a reconstruction which is invariant with respect to the applied basis. Hence, the randomized multiresolution decomposition enables localization of density fluctuations of various sizes within the deep interior part of the domain. Using simply the fine mesh shows any

Fig. 4. A schematic visualization of the data flow in the randomized multiresolution scan. The average of the MAP estimates obtained for the k-th multiresolution decomposition is used as the initial guess for the $k + 1$-th one.

density anomalies only on the surface of the reconstruction. The coarser mesh decomposition and randomized scanning algorithm average out errors due to discretization arising in the decomposition process.

2.6. Numerical implementation with Geoceles interface

The present forward and inverse algorithms can be found implemented in the open Geoceles software package (Geoceles interface, 2018) for the Matlab (Mathworks, Inc.) platform. The software was developed over the course of this study and was applied in the numerical experiments. Geoceles creates a regular tetrahedral mesh conforming to the segmentation determined by the closed triangular surfaces. It applies graphics processing unit (GPU) acceleration which is essential in order to reduce computation time with reasonably high tetrahedral mesh resolution.

2.7. Numerical experiments

In the numerical experiments, we investigated the effects of the (i) noise, (ii) measurement distance, (iii) point distribution (angular coverage), (iv) number of IAS iteration steps, (v) the resolution (sparsity factor), (vi) number of the multiresolution decompositions and (vii) resolution levels, as well as (viii) anomaly density. The specifications of the features (i)–(vii) can be found in Table 3. The numerical experiments were organized into four entities devoted to (**1**) orbit, (**2**) noise, (**3**) number of multiresolution decompositions, as well as (**4**) resolution and estimate type. These focused on different features as described in Table 4.

The likelihood standard deviation was selected to match with that of the relative standard deviation of the gravity gradient field magnitude. Gamma distribution was used as the hyperprior in the inversion process. The shape parameter β was set to 1.5 based on preliminary experimentation with the prior in these types of inversion tasks, and the scaling parameter θ_0 was chosen based on the visual inspection of reconstruction quality (location and size of the detected anomaly in the reconstruction). The values were normalized with respect to the maximum entry. The workable values of θ_0 at the lower noise levels were found to be 10^5 and 10^8 for the 305 and 500 m radii orbits, respectively. These values produced an appropriate reconstruction quality in comparison to the exact model. The higher value was required for the high noise and low resolution cases. For the very low resolution, high noise, and higher orbit cases the scaling parameter had to be adjusted to 10^{10} in order to obtain a reasonable reconstruction showing the anomaly. The value of θ_0 affects the shape of the prior and, consequently, also the MAP estimates. The higher values enhanced the reconstruction and, therefore, they were used in the inversion process.

3. Results

3.1. Measurement data

The magnitude and direction of the simulated scalar gravity field

Table 3
Specifications of the features (i)–(viii) compared in the numerical experiments.

Item	Parameter	Values			
(i)	Noise	(a): 2 E	(b): 8 E	(c): 80 E	(d): 800 E
(ii)	Orbit radius	500 m	305 m		
(iii)	Angular coverage	70°	30°		
(iv)	IAS iterations n_{IAS}	1	5	10	
	(Estimate type)	ℓ^2	ℓ^1		
(v)	Sparsity factor s	8	4	0	
(vi)	Number of decompositions	100	10	1	
(vii)	Number of resolutions	3	1		
(viii)	Anomaly density	Low (0 g/cm³)		High (8.0 g/cm³)	
(ix)	Positional uncertainty			5°	10°

Table 4
Numerical experiments (**1**)–(**4**).

Experiment	Title	Features investigated
(**1**)	Measurement configuration	(ii), (iii), (viii)
(**2**)	Noise level	(i), (ii)
(**3**)	Multiresolution scanning	(ii), (vi)
(**4**)	Estimate type	(iv), (v), (vii)

gradient is shown in the Fig. 5 for both measurement distances. The data shows clearly, how the strength of the field varies between the two models and the orbit distances, and that the difference is generally tangential. The high-density anomaly in the Model (B) causes more than five times higher field strengths in comparison to the Model (A) which contained two voids inside the asteroid. The measurement distance has an effect on, not just the magnitude of the field strength, but also on the localization of the anomalies. While there is clear localization of the signal in the lower orbit, similar effect is not seen as clearly in the more distant one, suggesting that a field originating from a distant source is averaged over the distance. The effect of the high-density anomaly in the Model (B) is clear in the 305 m orbit case. The field strength for Model (A) is generally more evenly distributed than for (B). However, that is to be expected as the mass distribution of (A) is more symmetric in comparison to (B).

Fig. 6 shows the projected data, which follows from multiplying the reconstruction with the system matrix, and also the residual, i.e., the difference between the actual and projected data, for the measurement distance of 500 m. The residual is obviously more random than the original data, which is in agreement with the current forward model in which the residual coincides with the noise term. The location of the largest amplitude is similar in each case, suggesting that the residual includes a model-driven component, which is not predicted by the present white noise error model.

3.2. Quality of reconstructions

The quality of reconstructions was inspected visually by examining how well the different parts of the exact models (A) and (B) (Fig. 1) were visible in the reconstructions. The size, shape and location of any density

anomalies indicated by the reconstructions were compared with the exact model. The good quality reconstructions showed clear, spherical anomalies of the size of the exact model, in the correct locations. The surface layer was not clearly distinguishable in any of the reconstructions.

3.3. Measurement configuration

In the experiment (**1**), the visually assessed quality of the reconstruction was affected more by the distance between the target and the measurement points than the point coverage of the measurements, as shown by the Fig. 7 depicting the orbits with 305 and 500 m radii. Distinguishing both low and high density anomalies, i.e., voids and boulders in the models (A) and (B), respectively, was found to be feasible at both distances. The closer, 305 m, orbit was observed to provide a superior depth localization capability, as the reconstructions obtained at 500 m distance were somewhat biased towards the surface of the target domain, which is shown by the greater spread of the anomaly detected.

3.4. Noise level

The signal-to-noise ratio (SNR) for Model (A) varied from poor 12 dB to appropriate 24 dB, and for Model (B) it was generally appropriate, ranging from 20 to 29 dB. The SNR for each case can be found in the Table 5

The effect of the noise level was investigated for the 500 m orbit in the experiment (**2**) the results of which can be found in Fig. 9. Anomaly detection was found to be feasible with the lowest noise level (a) for Models(A) and (B). Above that, the voids found for Model (A) were barely distinguished as such. Detection of the high density anomaly in Model (B) was less affected by the noise. However, the noise level (d) was too large for finding an appropriate reconstruction also in the case of (B).

3.5. Measurement arc

Realistic gravity gradient field measurements result in measurement arcs instead of points, causing positional uncertainty in the inversion stage. The effect of such uncertainty on the reconstruction is presented
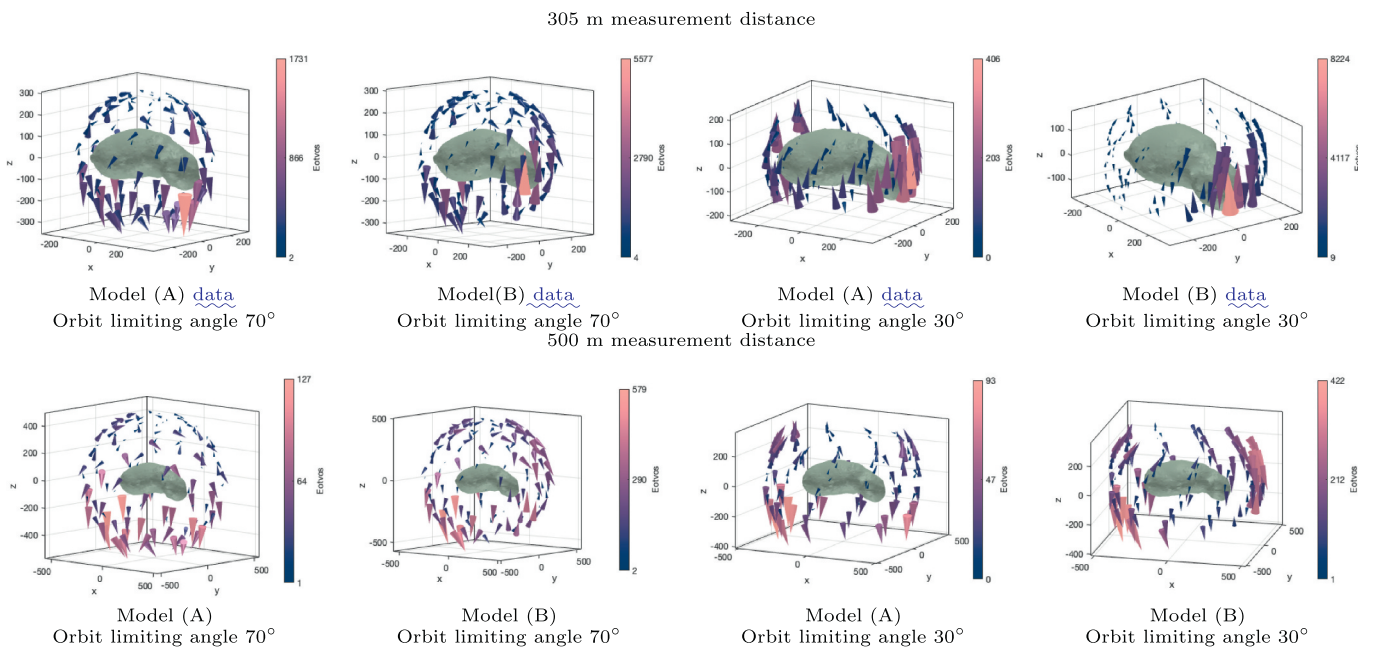
305 m measurement distance

| Model (A) data | Model(B) data | Model (A) data | Model (B) data |
| Orbit limiting angle 70° | Orbit limiting angle 70° | Orbit limiting angle 30° | Orbit limiting angle 30° |

500 m measurement distance

| Model (A) | Model (B) | Model (A) | Model (B) |
| Orbit limiting angle 70° | Orbit limiting angle 70° | Orbit limiting angle 30° | Orbit limiting angle 30° |

Fig. 5. The magnitude and direction of the scalar gravity field gradient at the measurement points depicted for each measurement configuration and both measurement distances.
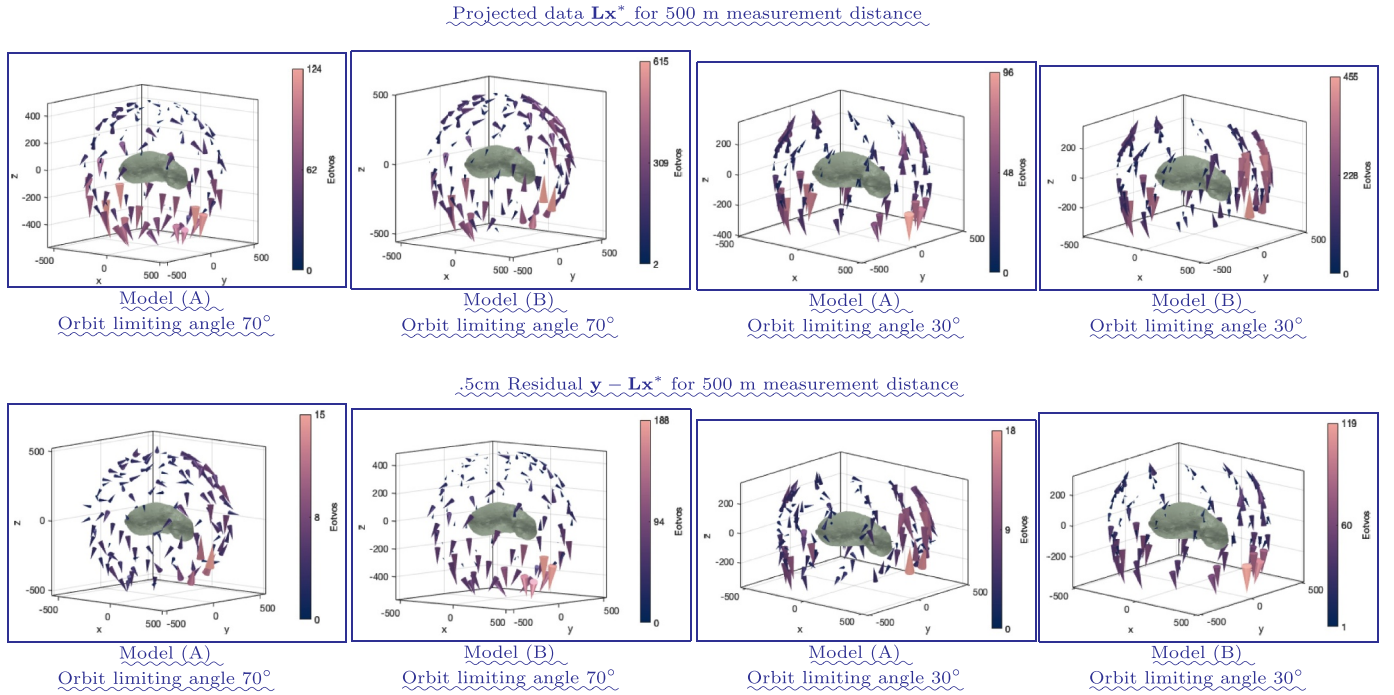
Projected data **L x*** for 500 m measurement distance

Model (A)
Orbit limiting angle 70°

Model (B)
Orbit limiting angle 70°

Model (A)
Orbit limiting angle 30°

Model (B)
Orbit limiting angle 30°

.5cm Residual **y** − **L x*** for 500 m measurement distance

Model (A)
Orbit limiting angle 70°

Model (B)
Orbit limiting angle 70°

Model (A)
Orbit limiting angle 30°

Model (B)
Orbit limiting angle 30°

Fig. 6. The projected data **L x*** and the residual **y** −**L x*** for the 500 m measurement distance. Here the reconstruction has been normalized so that the 2-norm of the actual and projected data coincide.

305 m measurement distance

Model (A)
Orbit limiting angle 70°

Model(B)
Orbit limiting angle 70°

Model (A)
Orbit limiting angle 30°

Model (B)
Orbit limiting angle 30°

.5cm 500 m measurement distance

Model (A)
Orbit limiting angle 70°

Model (B)
Orbit limiting angle 70°

Model (A)
Orbit limiting angle 30°
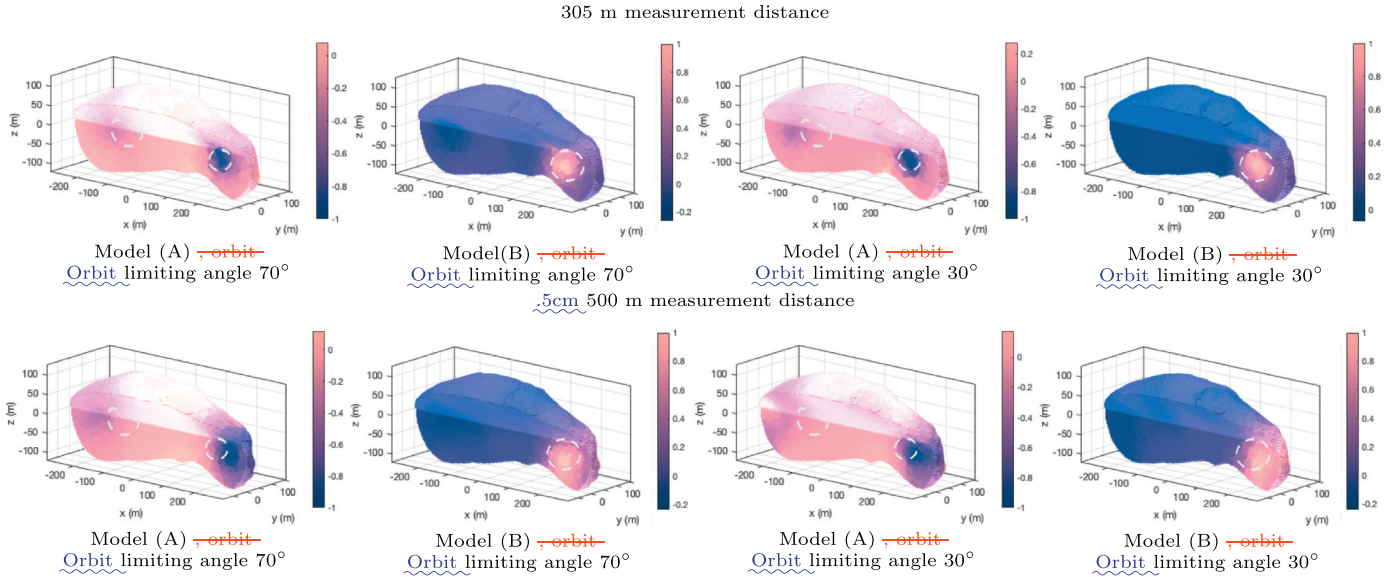
Model (B)
Orbit limiting angle 30°

Fig. 7. 3D cut-in views of the reconstructions at 305 and 500 m measurement distances and two different angular coverages with the corresponding measurement points shown in the Fig. 2. The higher coverage of points around the asteroid (limiting angle 70°) results in better localization of the perturbation at the higher orbit radius. With the smaller radius the effect on the reconstructions is not significant. The exact locations of the density anomalies are indicated with dashed white circles.

Table 5

Signal-to-noise ratios (SNR) for the investigated models. The SNR for the Model (A) varies from poor to acceptable, whereas for the Model (B) it is generally appropriate.

θ	r (m)	Model (A)	Model (B)
70°	305	24 dB	28 dB
	500	14 dB	21 dB
30°	305	21 dB	29 dB
	500	12 dB	20 dB

in the Fig. 8 for the 500 m measurement radius. The reconstruction quality for Model (A) was found to suffer from the positional uncertainty more than that found for Model (B).

3.6. Multiresolution scanning

The effects related to the number and sparsity factor of the multi-resolution decompositions were explored in the experiment (**3**) and are illustrated in the Fig. 9. The smoothest results were obtained using 100 decompositions and the sparsity factor $s = 8$. With a lower value $s = 4$, i.
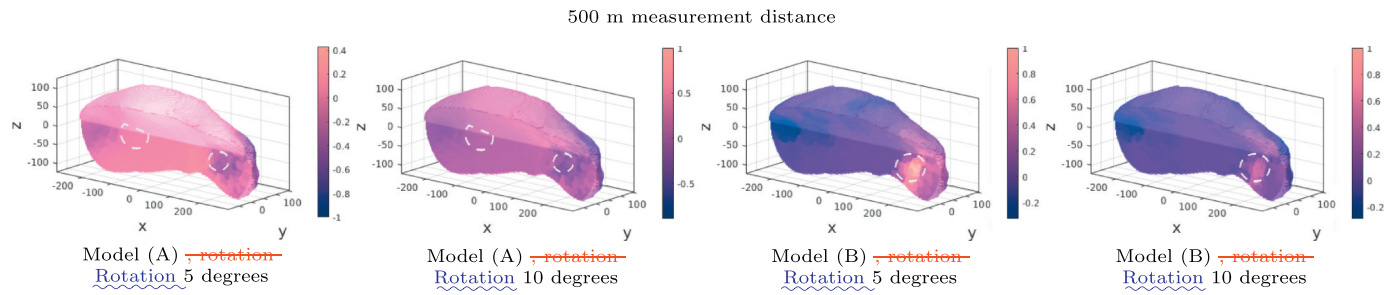
Fig. 8. The effect of positional uncertainty on the reconstructions. Such uncertainty results from measurements being carried out on a measurement arc instead of points. The exact locations of the density anomalies are indicated with dashed white circles.
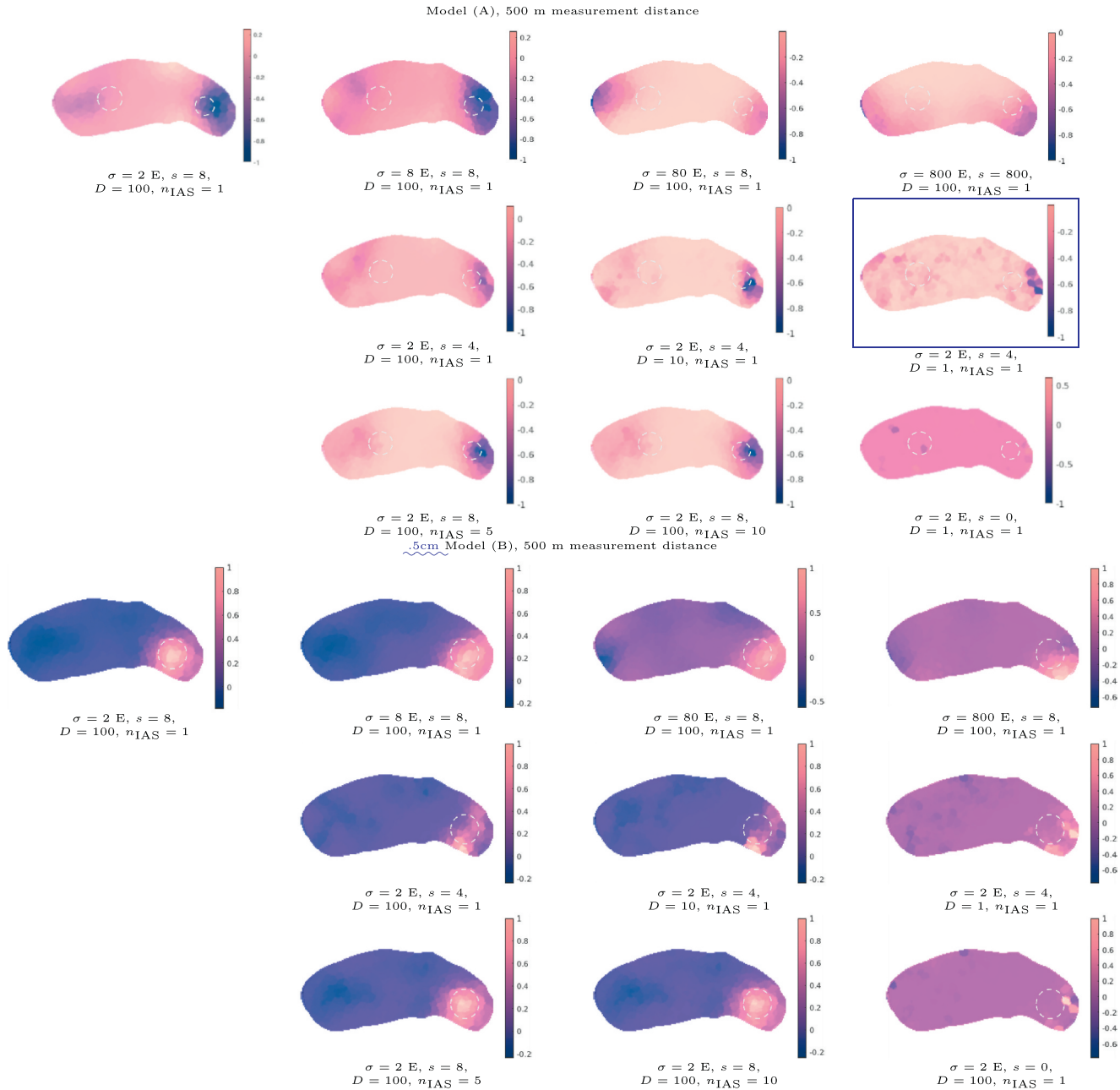

Fig. 9. The xz-plane crosscut views of the effects of noise level, sparsity factor, and IAS MAP iteration rounds n_{IAS} on the Model (A) and (B) reconstructions at 500 m measurement distance. The white dashed lines indicate the locations of the density anomalies. Parameters σ, s and D denote the standard deviation of the noise, the sparsity factor and the number of the multiresolution decompositions, respectively. The number of resolution levels is $L = 3$ in each case, and the number of IAS MAP iterations n_{IAS} performed for each level is identical. Sparsity 0 refers to a case in which the multiresolution decomposition was absent in the reconstruction process.

e., with a smaller difference between the coarse and fine resolution levels, the reconstructions became biased towards the surface, losing depth-resolution, and regularity regarding the shape of the detected anomalies. The irregularity and bias were found to be further exaggerated, when a lower number of decompositions (10 and 1) were used. The reconstructions obtained with a single decomposition also included some visible high-frequency artifact patterns which, otherwise, were essentially absent.

3.7. Estimate type

A comparison between ℓ^2 and ℓ^1 estimate types (**4**) can also be found in Fig. 9. The ℓ^2 estimate, obtained with $n_{IAS} = 1$, provided, overall, the most regular (smooth) outcome. Increasing the number of IAS iterations, i.e., finding an ℓ^1 type reconstruction, was observed to result in a sharper localization of the anomalies, sharpening also the other structures. The difference between the iteration counts of $n_{IAS} = 5$ and $n_{IAS} = 10$ was found to be a minor one. The essence of the multiresolution approach for the reconstruction quality is reflected by the single-resolution ℓ^2-reconstruction ($n_{IAS} = 1$ with a single resolution level) which suffers from an extreme surface bias and artifacts.

4. Discussion

Direct measurements of asteroid interiors have yet not been carried out (Herique et al., 2017) and, therefore, our understanding of the internal structures are based on bulk properties, asteroid spin rates, as well as on impact and other simulation studies suggesting candidate examples of structures fitting to the parameters. For example, the asteroid Itokawa is known to have a 40 % bulk porosity (Saito et al., 2006; Sanchez and Scheeres, 2014) and a potential aggregate structure (Barnouin-Jha et al., 2008) . The distribution of mass inside an asteroid is yet still mainly unknown. Our study suggests that the gradient of the gravity field can provide meaningful data of the internal distribution of mass, and that the data can be used for tomographic inversion.

The two synthetic models developed for this study were selected based on the confirmed bulk parameters for the asteroid Itokawa, and on possible scenarios how these properties can be achieved, to provide baseline information on the kinds of deep interior structures that can be observed from the orbit. The results obtained in Lowry, S. C. et al. (2014) suggest that Itokawa is composed of the merger of two separate bodies with bulk densities of $1.750 \pm 0.110\,\mathrm{g/cm^3}$ and $2.850 \pm 0.500\,\mathrm{g/cm^3}$. They used the shape model of Gaskell et al. (2008) which was based on rotational light curve analysis and applied detailed thermophysical analysis to the shape determined by the Hayabusa spacecraft (Saito et al., 2006) .

The double-void synthetic Model (A) corresponds to a low-density asteroid with significant void space in the interior. The high-density anomaly contained by the Model (B) corresponds to one possible formation scenario of Lowry, S. C. et al. (2014) , a catastrophic collision on a differentiated large object which contained a high-density metallic fragment (e.g. iron) in this formation process. This fragment could then have been subsumed by the silicate material in the "head" region. Although it is unlikely that two unrelated objects would have a sufficiently low-velocity encounter to ensure the survival of both lobes and still have uniform surface composition and structure on the two lobes, and assumption of the existence of such iron-containing lobe has not been verified by direct measurements, the suggested model was included in this study to examine the reconstruction of such a high-density anomaly by gravity gradient field inversion.

The insensitivity of the depth localization for the measurement distance observed in this study is a well-known feature in ground based gravity inversion applications (Erkan and Jekeli, 2011; Madej, 2017) . An obvious reason for this finding is the inherent ambiguity of depth information in gravity field data. Consequently, a nearby low-intensity anomaly can result in almost identical measurements with an outcome

following from a higher-intensity and more distant obstacle. As a result, fluctuations in the depth (radial) direction are difficult to be reconstructed. That is, when a vector corresponding to such a fluctuation is multiplied with the governing matrix **L** of the forward model, the resulting vector is likely to belong into the numerical null-space of **L** (Liu et al., 1995; Pursiainen, 2008) , meaning that it can have a norm very close to zero and making it weakly distinguishable based on the measurements. In the inversion stage, the weak depth-localization capability of the gravity data causes a strong bias of the reconstructions towards the surface of the target body which is why surface projections are used in presenting the results of gravity measurements, for example, the gravity acceleration on the surface of Mars in Gorski et al. (2018). The surface bias of a reconstruction is also a general phenomenon in inverse problems involving weak depth data, such as the biomedical imaging applications based on quasi-static electric field measurements (Calvetti et al., 2009; Kaipio and Somersalo, 2004) .

The essence of the proposed randomized multiresolution scan inversion approach is that the coarse density fluctuations are likely to be the clearest distinguishable components of the candidate solution set. Therefore, separating the coarse and fine details during the inversion process can provide an enhanced robustness of the final reconstruction compared to the approaches using all components at once. Here this is, especially, the case with correcting the bias in the depth direction. However, inverting measurements with a coarse discretization instead of a fine one might introduce other biases or artifacts relating to spatial location which in the present scanning approach are tackled by averaging the estimates produced by the IAS iteration over the set of randomized decompositions. The eventual inversion process can detect density details of various sizes as it can operate over a wide range of resolutions, and does not necessitate fixing the resolution *a priori* based on the deemed anomaly size.

Obtaining data from a close enough distance will obviously require a special mission design. A close approach for gravity measurement has been suggested, e.g., for Juventas CubeSat in Karatekin and Goldberg (2018). Maneuvering in the close proximity of the target will be difficult due to the inhomogeneities of the gravity field and, therefore, performing effective gravity field or gravity gradient measurements in the close proximity to a target SSSB will be challenging. Investigating realistic stable orbits around small bodies for gravimetric measurements will, therefore, be an important future research topic. A measurement duration of 5000 s resulting in a noise RMS of 4 E has been suggested to be feasible in Carroll and Faber (2018). Also incorporating the measurement arc instead of the point-approximation of the measurement used in this study and finding ways to incorporate model-driven components in the error model will be studied in the future. Obtaining a sufficiently low noise might be also possible via a radio-scientific Doppler shift measurement. Such approach was utilized, for example, in the high-precision measurements of the recent lunar science mission GRAIL (Gravity Recovery and Interior Laboratory) with two spacecraft configuration (Andrews-Hanna et al., 2013; Konopliv et al., 2013; Zuber et al., 2013) . In addition to the signal specifications, the accuracy of a Doppler measurement will be limited also by external factors such as the solar wind pressure which presents a challenge with SSSBs of the size such as Itokawa and other asteroids with a few hundred meter diameters.

Another important direction for the future work will be to investigate parallel radar and gravity inversion. Akin to the ground-based geoimaging applications (Erkan and Jekeli, 2011; Hausmann et al., 2007; Mochales et al., 2008) , a radar-based reconstruction of the interior structure may be expected to provide a superior depth-resolution compared to gravimetry, since the electromagnetic wave of the radar signal carries time-domain information which enables depth-inference of the scattering obstacle. Hence, a radar observation will be also less dependent on the observation distance in comparison to gravity measurements. Our recent findings suggest that radar inversion emphasizes high-contrast details with the cost of smooth variations such as large

areas of denser or more porous regolith which might be detected by a gravimeter (Sorsa et al., in press) . Therefore, it will also be vital to analyze the interconnection and correlation between the electric permittivity and mass density distributions observed by the radar and gravimeter, respectively (Trabelsi et al., 2001) . Validating the gravity gradiometry inversion approach proposed in this paper with measurements in a terrestial application such as suggested by Kirkendall, Barry et al. (2007) is also a potential future work topic.

5. Conclusion

This article concentrated on the mathematical methodology, resolution, noise and orbit radius selection with tomographic gravity field investigation performed for an asteroid as the potential application. The results obtained with simulated data suggest that the randomized multiresolution scanning technique combined with the iterative alternating sequential (IAS) inversion algorithm provides an advantageous way to enable depth localization of density anomalies, a feature not inherent in other inversion methods.

Void localization in an asteroid would require the measurement noise to be below 8 E at 500 m orbit. The reconstruction of a high-density anomaly is less sensitive to noise, and it can be achieved with noise levels up to 80 E. This is also reflected in the signal-to-noise ratios obtained for the models. The reconstruction method was shown to be robust with respect to the positional uncertainty of the measurement for up to 5% error, confirming long enough measurement times to be able to reduce the measurement noise in real measurement scenarios.

Acknowledgments

References

Andrews-Hanna, J.C., Asmar, S.W., Head, J.W., Kiefer, W.S., Konopliv, A.S., Lemoine, F.G., Matsuyama, I., Mazarico, E., McGovern, P.J., Melosh, H.J., et al., 2013. Ancient igneous intrusions and early expansion of the moon revealed by grail gravity gradiometry. Science 339, 675–678.

Barnouin-Jha, O.S., Cheng, A.F., Mukai, T., Abe, S., Hirata, N., Nakamura, R., Gaskell, R.W., Saito, J., Clark, B.E., 2008. Small-scale topography of 25143 Itokawa from the Hayabusa laser altimeter. Icarus 198, 108–124.

Binzel, R.P., Rivkin, A.S., Bus, S.J., Sunshine, J.M., Burbine, T.H., 2001. Muses-c target asteroid (25143) 1998 sf36: a reddened ordinary chondrite. Meteorit. Planet. Sci. 36, 1167–1172.

Braess, D., 2007. Finite Elements: Theory, Fast Solvers, and Applications in Solid Mechanics. Cambridge University Press.

Bridson, R. Fast poisson disk sampling in arbitrary dimensionsPlease supply the year of publication in "Bridson".. http://www.cs.ubc.ca/rbridson/docs/bridson-siggraph07-poissondisk.pdf. ???? Accessed: 17 May 2019.

Calvetti, D., Hakula, H., Pursiainen, S., Somersalo, E., 2009. Conditionally Gaussian hypermodels for cerebral source localization. SIAM J. Imag. Sci. 2, 879–909.

Calvetti, D., Somersalo, E., 2008. Hypermodels in the Bayesian imaging framework. Inverse Prob. 24, 034013.

Carroll, K., Faber, D., 2018. Tidal Acceleration Gravity Gradiometry for Measuring Asteroid Gravity Field from Orbit. https://www.researchgate.net/publication/328828084_Tidal_Acceleration_Gravity_Gradiometry_for_Measuring_Asteroid_Gravity_Field_From_Orbit.

Carroll, K., Zee, R., Spencer, H., Connors, M., 2018. Geophysical Reconnaissance Asteroid Surface Probe (GRASP). https://www.researchgate.net/publication/328828150_Geophysical_Reconnaissance_Asteroid_Surface_Probe_GRASP.

Carry, B., 2012. Density of asteroids. Planet. Space Sci. 73, 98–118.

Chromk, J., Grin, M., Panisova, J., Vajda, P., Kubov, A., 2016. Validation of sensitivity and reliability of gpr and microgravity detection of underground cavities in complex urban settings: test case of a cellar. Contributions to Geophysics and Geodesy 46.

Cignoni, P., Callieri, M., Corsini, M., Dellepiane, M., Ganovelli, F., Ranzuglia, G., 2008. MeshLab: An Open-Source Mesh Processing Tool. In: Scarano, V., Chiara, R.D., Erra, U. (Eds.), Eurographics Italian Chapter Conference. The Eurographics Association.

Deller, J.F., 2017. Hyper-Velocity Impacts on Rubble Pile Asteroids. Ph.D. thesis. School of Physical Sciences University of Kent Canterbury U.K. and International Max Planck Research School for Solar System Science Göttingen Germany.

Erkan, K., Jekeli, C., 2011. A comparative analysis of geophysical fields for multi-sensor applications. J. Appl. Geophys. 74, 142–150.

Fujiwara, A., Kawaguchi, J., Yeomans, D.K., Abe, M., Mukai, T., Okada, T., Saito, J., Yano, H., Yoshikawa, M., Scheeres, D.J., Barnouin-Jha, O., Cheng, A.F., Demura, H., Gaskell, R.W., Hirata, N., Ikeda, H., Kominato, T., Miyamoto, H., Nakamura, A.M., Nakamura, R., Sasaki, S., Uesugi, K., 2006. The rubble-pile asteroid Itokawa as observed by Hayabusa. Science 312 (5778), 1330–1334.

Gaskell, R., Saito, J., Ishiguro, M., Kubota, T., Hashimoto, T., Hirata, N., Abe, S., Barnouin-Jha, O., Scheeres, D., 2008. Gaskell Itokawa Shape Model v1.0. HAY-A-AMICA-5-ITOKAWASHAPE-V1.0. NASA Planetary Data System.

Geoceles interface, 2018. Geoimaging Tool for Small Celestial Bodies. https://github.com/sampsapursiainen/Geoceles [Accessed 5 December 2018].

Gorski, K.M., Bills, B.G., Konopliv, A.S., 2018. A high resolution mars surface gravity grid. Planet. Space Sci. 160, 84–106.

Hausmann, H., Krainer, K., Brckl, E., Mostler, W., 2007. Internal structure and ice content of Reichenkar rock glacier (Stubai Alps, Austria) assessed by geophysical investigations. Permafr. Periglac. Process. 18, 351–367.

Hayabusa Project Science Data Archive, 2007. Itokawa Shape Model. https://darts.isas.jaxa.jp/planet/project/hayabusa/shape.pl. Accessed 18 December, 2017.

Herique, A., Agnus, B., Asphaug, E., Barucci, A., Beck, P., Bellerose, J., Biele, J., Bonal, L., Bousquet, P., Bruzzone, L., Buck, C., Carnelli, I., Cheng, A., Ciarletti, V., Delbo, M., Du, J., Du, X., Eyraud, C., Fa, W., Fernandez, J.G., Gassot, O., Granados-Alfaro, R., Green, S., Grieger, B., Grundmann, J., Grygorczuk, J., Hahnel, R., Heggy, E., Ho, T.-M., Karatekin, O., Kasaba, Y., Kobayashi, T., Kofman, W., Krause, C., Kumamoto, A., Kuppers, M., Laabs, M., Lange, C., Lasue, J., Levasseur-Regourd, A., Mallet, A., Michel, P., Mottola, S., Murdoch, N., Mutze, M., Oberst, J., Orosei, R., Plettemeier, D., Rochat, S., RodriguezSuquet, R., Rogez, Y., Schaffer, P., Snodgrass, C., Souyris, J.-C., Tokarz, M., Ulamec, S., Wahlund, J.-E., Zine, S., 2017. Direct observations of asteroid interior and regolith structure: Science measurement requirements. Adv. Space Res.

Japan Aerospace Exploration Agency, 2003. Hayabusa Project. http://global.jaxa.jp/projects/sat/muses_c/index.html [Accessed 18 January 2018].

Jekeli, C., Lian Abt, J., 2011. Locating anomalies by gravity gradiometry using the matched filter with a probabilistic assessment. Stud. Geophys. Geod. 55, 1–19.

Jutzi, M., Benz, W., 2017. Formation of bi-lobed shapes by sub-catastrophic collisions. A late origin of comet 67P's structure. Astron. Astrophys. 597, A62.

Kaipio, J., Somersalo, E., 2004. Statistical and Computational Inverse Problems. Springer-Verlag New York.

Karatekin, Ö., Goldberg, H., 2018, November. Juventas cubesat. In: Hera community workshop 15-16 November 2018. https://www.cosmos.esa.int/documents/1786001/1846091/7.+juventas-overview_v3.pdf/b548e67a-9243-9263-96d7-60d643f8f8e1.

Kirkendall, Barry, Li, Yaoguo, Oldenburg, Doublas, 2007. Imaging cargo containers using gravity gradiometry. IEEE Trans. Geosci. Remote Sens. 45, 1786–1797.

Kofman, W., Barbin, Y., Klinger, J., Levasseur-Regourd, A.-C., Barriot, J.-P., Herique, A., Hagfors, T., Nielsen, E., Grn, E., Edenhofer, P., Kochan, H., Picardi, G., Seu, R., van Zyl, J., Elachi, C., Melosh, J., Veverka, J., Weissman, P., Svedhem, L., Hamran, S., Williams, I., 1998. Comet nucleus sounding experiment by radiowave transmission. Adv. Space Res. 21, 1589–1598.

Kofman, W., Herique, A., Barbin, Y., Barriot, J.-P., Ciarletti, V., Clifford, S., Edenhofer, P., Elachi, C., Eyraud, C., Goutail, J.-P., Heggy, E., Jorda, L., Lasue, J., Levasseur-Regourd, A.-C., Nielsen, E., Pasquero, P., Preusker, F., Puget, P., Plettemeier, D., Rogez, Y., Sierks, H., Statz, C., Svedhem, H., Williams, I., Zine, S., Van Zyl, J., 2015. Properties of the 67p/Churyumov-Gerasimenko interior revealed by consert radar. Science 349.

Kofman, W., Herique, A., Goutail, J.-P., Hagfors, T., Williams, I.P., Nielsen, E., Barriot, J.-P., Barbin, Y., Elachi, C., Edenhofer, P., Levasseur-Regourd, A.-C., Plettemeier, D., Picardi, G., Seu, R., Svedhem, V., 2007. The comet nucleus sounding experiment by radiowave transmission (consert): a short description of the instrument and of the commissioning stages. Space Sci. Rev. 128, 413–432.

Konopliv, A.S., Park, R.S., Yuan, D.-N., Asmar, S.W., Watkins, M.M., Williams, J.G., Fahnestock, E., Kruizinga, G., Paik, M., Strekalov, D., et al., 2013. The jpl lunar gravity field to spherical harmonic degree 660 from the grail primary mission. J. Geophys. Res. Planets 118, 1415–1434.

Lauretta, D.S., Balram-Knutson, S.S., Beshore, E., Boynton, W.V., Drouet d'Aubigny, C., DellaGiustina, D.N., Enos, H.L., Golish, D.R., Hergenrother, C.W., Howell, E.S., Bennett, C.A., Morton, E.T., Nolan, M., Rizk, B., Roper, H.L., Bartels, A.E., Bos, B.J., Dworkin, J.P., Highsmith, D.E., Lorenz, D.A., Lim, L.F., Mink, R., Moreau, M.C., Nuth, J.A., Reuter, D.C., Simon, A.A., Bierhaus, E.B., Bryan, B.H., Ballouz, R., Barnouin, O.S., Binzel, R.P., Bottke, W.F., Hamilton, V.E., Walsh, K.J., Chesley, S.R., Christensen, P.R., Clark, B.E., Connolly, H.C., Crombie, M.K., Daly, M.G., Emery, J.P., McCoy, T.J., McMahon, J.W., Scheeres, D.J., Messenger, S., Nakamura-Messenger, K., Righter, K., Sandford, S.A., 2017. Osiris-rex: sample return from asteroid (101955) bennu. Space Sci. Rev. 212, 925–984.

Liu, Y., Guenier, B., Benard, C., 1995, Dec. A sensitivity decomposition for the regularized solution of inverse heat conduction problems by wavelets. Inverse Prob. 11, 1177–1187.

Lowry, S.C., Weissman, P.R., Duddy, S.R., Rozitis, B., Fitzsimmons, A., Green, S.F., Hicks, M.D., Snodgrass, C., Wolters, S.D., Chesley, S.R., Pittichová, J., van Oers, P., 2014. The internal structure of asteroid (25143) Itokawa as revealed by detection of yorp spin-up. A&A 562, A48.

Madej, J., 2017. Gravimetric surveys for assessing rock mass condition around a mine shaft. Acta Geophys. 65, 465–479.

McKenna, J.R., Rim, H., Li, Y., 2016. Feasibility and limitations of void detection using gravity gradiometry. IEEE Trans. Geosci. Remote Sens. 54, 881–891.

Mochales, T., Casas, A.M., Pueyo, E.L., Pueyo, O., Román, M.T., Pocoví, A., Soriano, M.A., Ansón, D., 2008. Detection of underground cavities by combining gravity,

magnetic and ground penetrating radar surveys: a case study from the Zaragoza area, NE Spain. Environ. Geol. 53, 1067–1077.

Nakamura, T., Noguchi, T., Tanaka, M., Zolensky, M.E., Kimura, M., Tsuchiyama, A., Nakato, A., Ogami, T., Ishida, H., Uesugi, M., Yada, T., Shirai, K., Fujimura, A., Okazaki, R., Sandford, S.A., Ishibashi, Y., Abe, M., Okada, T., Ueno, M., Mukai, T., Yoshikawa, M., Kawaguchi, J., 2011. Itokawa dust particles: a direct link between s-type asteroids and ordinary chondrites. Science 333, 1113–1116.

Okada, T., Shirai, K., Yamamoto, Y., Arai, T., Ogawa, K., Hosono, K., Kato, M., 2006. X-ray fluorescence spectrometry of asteroid Itokawa by Hayabusa. Science 312, 1338–1341.

Panisova, J., Fratia, M., Wunderlich, T., Pateka, R., Kunirk, D., 2013. Microgravity and ground-penetrating radar investigations of subsurface features at the St Catherine's Monastery, Slovakia. Archaeol. Prospect. 20, 163–174.

Pursiainen, S., 2008, 12. Coarse-to-fine reconstruction in linear inverse problems with application to limited-angle computerized tomography. Journal of Inverse and Ill-posed Problems 16, 873–886.

Pursiainen, S., Kaasalainen, M., 2013. Iterative alternating sequential (ias) method for radio tomography of asteroids in 3d. Planet. Space Sci. 82, 84–98.

Saito, J., Miyamoto, H., Nakamura, R., Ishiguro, M., Michikami, T., Nakamura, A.M., Demura, H., Sasaki, S., Hirata, N., Honda, C., Yamamoto, A., Yokota, Y., Fuse, T., Yoshida, F., Tholen, D.J., Gaskell, R.W., Hashimoto, T., Kubota, T., Higuchi, Y., Nakamura, T., Smith, P., Hiraoka, K., Honda, T., Kobayashi, S., Furuya, M., Matsumoto, N., Nemoto, E., Yukishita, A., Kitazato, K., Dermawan, B., Sogame, A., Terazono, J., Shinohara, C., Akiyama, H., 2006. Detailed Images of Asteroid 25143 Itokawa from Hayabusa. Science 312, 1341–1344.

Sorsa, L.-I., Takala, M., Bambach, P., Deller, J., Vilenus, E., Pursiainen, S., 2019. Bistatic full-wave radar tomography detects deep interior voids, cracks and boulders in a rubble-pile asteroid model. The Astrophysical Journal 872 (1), 44.

Sanchez, P., Scheeres, D.J., 2014. The strength of regolith and rubble pile asteroids. Meteorit. Planet. Sci. 49, 788–811.

Takala, M., Bambach, P., Deller, J., Vilenus, E., Wittig, M., Lentz, H., Braun, H., Kaasalainen, M., Pursiainen, S., 2018. Far-field inversion for the deep interior scanning cubesat. IEEE Trans. Aerosp. Electron. Syst. 55 (4), 1683–1697.

Trabelsi, S., Kraszewski, A.W., Nelson, S.O., 2001. Microwave dielectric sensing of bulk density of granular materials. Meas. Sci. Technol. 12, 2192–2197.

Tsuchiyama, A., Uesugi, M., Matsushima, T., Michikami, T., Kadono, T., Nakamura, T., Uesugi, K., Nakano, T., Sandford, S.A., Noguchi, R., Matsumoto, T., Matsuno, J., Nagano, T., Imai, Y., Takeuchi, A., Suzuki, Y., Ogami, T., Katagiri, J., Ebihara, M., Ireland, T.R., Kitajima, F., Nagao, K., Naraoka, H., Noguchi, T., Okazaki, R., Yurimoto, H., Zolensky, M.E., Mukai, T., Abe, M., Yada, T., Fujimura, A., Yoshikawa, M., 2011. Three-dimensional structure of Hayabusa samples: origin and evolution of Itokawa regolith. Science 333, 1125–1128.

Tsuda, Y., Yoshikawa, M., Abe, M., Minamino, H., Nakazawa, S., 2013. System design of the Hayabusa 2 — asteroid sample return mission to 1999 ju3. Acta Astronaut. 91, 356–362.

Zuber, M.T., Smith, D.E., Watkins, M.M., Asmar, S.W., Konopliv, A.S., Lemoine, F.G., Melosh, H.J., Neumann, G.A., Phillips, R.J., Solomon, S.C., Wieczorek, M.A., Williams, J.G., Goossens, S.J., Kruizinga, G., Mazarico, E., Park, R.S., Yuan, D.-N., 2013. Gravity field of the moon from the gravity recovery and interior laboratory (grail) mission. Science 339, 668–671.